**Research Article**

# Identifying determinants of γ' phase coarsening behavior in Co/CoNi-based superalloys with explainable artificial intelligence (XAI)

Linlin Sun[1,2], Qingshuang Ma[1,2], Jingwen Zhang[3], Liming Yu[3], Jie Xiong[4,*] (iD), Huijun Li[5], Qiuzhi Gao[1,2,*] (iD)

[1]School of Materials Science and Engineering, Northeastern University, Shenyang 110819, Liaoning, China.
[2]School of Resources and Materials, Northeastern University at Qinhuangdao, Qinhuangdao 066004, Hebei, China.
[3]School of Materials Science and Engineering, Tianjin University, Tianjin 300354, China.
[4]Materials Genome Institute, Shanghai University, Shanghai 200444, China.
[5]Faculty of Engineering and Information Sciences, University of Wollongong, Wollongong 2522, Australia.

[*]**Correspondence to:** Dr. Jie Xiong, Materials Genome Institute, Shanghai University, 333 Nanchen Road, Shanghai 200444, China. E-mail: xiongjie@shu.edu.cn; Prof. Qiuzhi Gao, School of Materials Science and Engineering, Northeastern University, No.11, Lane 3, Wenhua Road, Shenyang 110819, Liaoning, China. E-mail: neuqgao@163.com

## Abstract

The coarsening of γ' phases in superalloys is influenced by multiple factors and significantly impacts mechanical properties, such as strength and creep resistance. While classical kinetic theory delineates the coarsening mechanisms of γ' phases, it has limitations when excessive coarsening occurs. The challenge of identifying the pivotal factors that markedly affect the kinetic behavior of γ' phase coarsening remains largely unresolved. This study utilized eXtreme Gradient Boosting (XGBoost) models to identify the CP and CPAE features that characterize the coarsening behavior of γ' phases in Co/CoNi-based superalloys. Through meticulous analysis of CP features [aging temperature ($T$), the atomic fraction of the Ti element ($c_{Ti}$), the atomic fraction of the V element ($c_V$), and the atomic fraction of the Ta element ($c_{Ta}$)] and CPAE features [$T$, Young's modulus ($E$), electronegativity ($EN$), atomic radius ($r$), $c_{Ti}$, the differences of atomic radius ($\sigma r$), and the differences of electronegativity ($\sigma EN$)], we derived explicit mathematical expressions using symbolic classification approach, which offers improved interpretability compared to traditional black-box models. Our findings indicate that $T$, $c_{Ti}$, $c_{Ta}$, $E$ and $\sigma r$ are dominant factors influencing γ' coarsening behavior across different Co/CoNi-based superalloys. Notably, $T$, $c_{Ti}$, $c_{Ta}$ and $\sigma r$ exhibit an inverse correlation with the γ' coarsening behavior, whereas $E$ shows a positive correlation. These insights provide valuable guidance for determining whether coarseningoccurs in newly designed alloys. Furthermore, they facilitate

the design of innovative anti-coarsening Co/CoNi-based superalloys. This knowledge is instrumental in enhancing alloy formulations, ensuring their performance and longevity in demanding environments where thermal stability is paramount.

## INTRODUCTION

Since the rediscovery of the $L1_2$-ordered γ'-$Co_3$ (Al, W) phase in the Co-Al-W alloy system by Sato *et al.*, Co-based superalloys have garnered significant attention as promising materials for high-temperature applications[1]. Subsequent studies[2-4] have demonstrated that γ'-strengthened Co-based superalloys possess comparable high-temperature creep strength, higher melting points, and a broader processing window than Ni-based superalloys. These advantages position them as promising candidates for next-generation high-temperature materials. Over the past decade, efforts to optimize these alloys have led to a transition from the initial Co-Al-W ternary systems to advanced multi-component CoNi-based alloys[5-7].

A critical factor influencing the high-temperature performance of Co/CoNi-based superalloys is the stability of their γ/γ' two-phase microstructure. Maintaining mechanical properties during high-temperature service requires that the γ/γ' dual-phase structure remains stable, with minimal precipitation of detrimental secondary phases, and that the γ' phase occurs slowly to prevent rapid degradation of mechanical properties. Generally, studies investigating γ' phase coarsening behavior within the γ/γ' two-phase region relied on experimental methods. While informative, these approaches are often time-consuming, costly, and limited by a narrow compositional range[8-10]. Furthermore, research on γ' phase coarsening typically requires long-term aging, often extending to several hundred or even over a thousand hours, which drastically increases both the time and cost of experimentation[11-13]. These limitations make it challenging to systematically explore the underlying mechanisms of γ' coarsening across a wide range of alloy compositions and processing conditions.

In recent years, data-driven machine learning (ML) techniques have made significant strides in studying and analyzing the microstructural evolution in Co/CoNi-based superalloys[14-16]. Various ML algorithms, such as image processing[15] and neural networks[17], have demonstrated exceptional capabilities in predicting the coarsening behavior of the γ' phase. Feature selection is crucial in ML models, as identifying the key factors influencing γ' phase coarsening behavior, which are derived from elemental compositions, process parameters, and microphysical characteristics, is fundamental to constructing effective predictive models. Recently, Liu *et al.* utilized image processing to extract microstructural information and developed a regression model correlating these features with γ' phase size, identifying factors influencing γ' phase size[15]. They inferred that the difference of Young's modulus ($E$) play a dominant role in the coarsening mechanism of γ' phases in Co/CoNi-based superalloys.

Despite these advancements, there remains considerable scope for further improvement in ML models to predict γ' phase coarsening behavior. Identifying additional critical features and incorporating explainable artificial intelligence (XAI) algorithms are essential steps forward, providing the motivation for the present study. Currently, widely used interpretable ML algorithms include SHapley Additive exPlanation (SHAP) analysis[18], local interpretable model-agnostic explanation (LIME)[19], and symbolic regression (SR)[17]. SR, in particular, is a prominent ML approach that derives explicit mathematical formulas from data. When combined with domain knowledge, SR generates physically meaningful analytical expressions, and it has been extensively applied in materials research[20-23]. However, its application has primarily focused on

regression problems, with minimal use in classification tasks.

In this study, we compiled a comprehensive dataset that encompasses constituent elemental compositions, process parameters, and atomic and electronic properties. Using the XGBoost algorithm, we developed a binary classification model to predict the coarsening behavior of the γ' phase. Key features affecting the coarsening process were identified through feature selection, providing deeper insights into the underlying mechanisms. Additionally, we employed a symbolic classification (SC) algorithm to derive explicit mathematical formulas for predicting γ' phase coarsening across various Co/CoNi-based superalloy systems and processing conditions, further enhancing the model's interpretability and practicality. Finally, the accuracy and practical applicability of the proposed ML model were validated using three candidate alloys. This research not only advances the understanding of γ' phase coarsening behavior in Co/CoNi-based superalloys but also provides an efficient and interpretable tool for alloy design.

## MATERIALS AND METHODS
### Data acquisition
We compiled a dataset of 132 experimental data points from the literature spanning from 2006 to the present, focusing on the coarsening rate constants ($K_r$) of γ' phases in Co/CoNi-based superalloys. Detailed information regarding the data sources is provided in the Supplementary Materials. This dataset includes ten common elements, Co, Ni, Al, W, Ta, Ti, Mo, Cr, V, and Nb, and the aging temperature ($T$) as a process parameter. The statistical distributions of these elemental compositions and the process parameter are presented in Supplementary Figure 1. Notably, refractory elements with large atomic sizes, such as Zr and Hf, and grain boundary strengthening elements such as B are excluded from the dataset.

Upon reviewing the literature, we observed variations in methodologies for calculating the γ' phase size, which directly influences $K_r$. Different studies have employed metrics such as half of the edge length[24,25], area-equivalent radius[2,13,15], volume-equivalent radius[26-28], and direct measurements of the edge lengths[29]. To address these inconsistencies, we standardized the measurement approach by adopting the volume-equivalent radius as a uniform measurement technique. The corresponding expression is:

$$r = a \left( \frac{3}{4\pi} \right)^{\frac{1}{3}}$$

(1)

Where $r$ is the equivalent precipitate radius of γ' precipitates assumed to be cubic-shaped, and $a$ is the cube edge length determined by measuring the square root of the average cross-sectional area obtained via Image Pro Plus software.

Three principal kinetic theories are widely accepted regarding the coarsening behaviors of the γ' phase in superalloys. The first, the Lifshitz-Slyozov-Wagner (LSW) theory[30], asserts that the coarsening process of precipitate phase particles is primarily controlled by the diffusion of solute atoms within the matrix. The second, the Trans-Interface Diffusion-Controlled (TIDC) theory[31], suggests that when the coarsening process involves both ordered and disordered interfaces (e.g., the γ/γ' phase interface), the rate at which solute atoms traverse these interfaces is governed by the interfaces themselves. The third theory highlights a competition between diffusion-controlled and interface-controlled coarsening behavior[32]. The theory posits that the coarsening mechanism of coherent γ' precipitate in γ matrices is usually affected by two factors: diffusion and interface reaction. These factors can be clearly reflected by particle size distributions (PSDs). Gusak *et al.* simulated non-equilibrium coarsening behaviors and proposed that the coarsening process can

be divided into three stages[33]. In the second stage, the coarsening exponent ranges between 2 and 3. The PSD obtained from simulations lies between LSW and Hillert theories. As the process enters the third stage, the coarsening law and PSD approach are closer to the LSW form, leading to the concept of coarsening transition. Subsequently, Sun found that different stages of the coarsening process are controlled by varying factors, namely diffusion and interface, and that there is a competitive relationship between these factors[34]. The distinctions among these theories can be illustrated by the following kinetic expression:

$$<r_t>^n - <r_0>^n = K_r(t - t_0)$$

(2)

where $<r_t>$ is the average equivalent γ' precipitate radius at time $t$, $<r_0>$ is the average equivalent γ' precipitate radius at the coarsening start time $t_0$, $K_r$ is the γ' phase coarsening rate constant, and $n$ is the time exponent of the γ' phase size. In the LSW theory and TIDC theory, the values of $n$ are 3 and 2, respectively. The value of $n$ can be determined through multiple nonlinear regression to ascertain which theoretical model more accurately describes the coarsening process of γ' phase in Co/CoNi-based superalloys.

Using the unified volume-equivalent radius, we calculated the time exponent $n$ for the γ' phase size of all 132 samples. The values of $n$ range from 1.1 to 5.6, with their statistical distribution illustrated in Supplementary Figure 1. Subsequently, the $K_r$ for the γ' phase was recalculated based on these $n$ values. Corresponding to the three kinetic theories mentioned earlier, our methodology is defined as follows: for $n \leq 2$, we adopt $n = 2$ to calculate $K_r$; for $2 < n < 3$, we use the actual value of $n$; for $n \geq 3$, we uniformly set $n = 3$. The statistical distribution of $K_r$ is also shown in Supplementary Figure 1, expressed in units of nm$^n$/s.

As can be seen, $K_r$ obeys a long-tailed distribution, leading to an unbalanced regression problem, and we thus segmented $K_r$ into two distinct categories to perform classifications for coarsening behaviors. Here, values of $K_r$ ranging from 0 to 1 are categorized as "Slow", while values exceeding 1 are classified as "Fast". The sample sizes for the "Slow" and "Fast" classes were 50 and 82, respectively. Both categories are collectively identified by the term $K_{cla}$, and utilized for constructing a classification ML model.

The $K_r$ given in Equation (2), when $n$ is 3, can be expressed as[35]:

$$K_r = \frac{8D_{eff}\sigma C_e V_m}{9RT}$$

(3)

where $D_{eff}$ is the effective diffusion coefficient of the solute element in the γ matrix, $\sigma$ is the γ/γ' interfacial energy, $C_e$ is the equilibrium solubility of the solute element in the γ matrix, $V_m$ is the molar volume fraction of γ' precipitates, $R$ is the gas constant (8.31 J/mol/K), and $T$ is the absolute temperature (K).

**Feature pool**

In alloy design, the constituent elements can be directly employed as features for inverse design, as demonstrated in the previous study[7]. Additionally, the atomic and electronic properties of these elements can serve as features, allowing for the generalization of constructed ML models. This approach enables alterations in constituent elements while preserving their atomic and electronic characteristics. In this study, we integrated the constituent elements and processing parameters (CP) as a unified set of input features. Moreover, the constituent elements, processing parameters, and nine atomic and electronic properties are analyzed collectively as a distinct and comprehensive set of input features (CPAE).

These atomic and electronic features which potentially influence the coarsening behavior of γ' phases were proposed based on domain knowledge, defined as follows:

$$\overline{f} = \sum_{i=1}^{n} c_i f_i \tag{4}$$

$$\sigma f = \sqrt{\sum_{i=1}^{n} c_i (\overline{f} - f_i)^2} \tag{5}$$

$$\Delta S = -R \sum_{i=1}^{n} c_i \ln c_i \tag{6}$$

where $c_i$ represent the atomic fraction of the $i$th element. $R$ is the gas constant. $\sigma f$ represent the differences of elemental properties. The elemental properties considered include $E$, atomic radius ($r$), electronegativity ($EN$), valence electron number ($VEN$), and configurational entropy ($\Delta S$).

**Feature selection and model training**
Decision tree ensembles, particularly the XGBoost algorithm, are considered highly effective for predicting superalloy properties due to their outstanding accuracy[36-39]. XGBoost enhances model performance by constructing multiple decision trees and optimizing them through gradient boosting ensemble techniques[40]. Hence, the algorithm was employed to construct ML models in the present work.

In conjunction with the XGBoost algorithm, the sequential backward selector (SBS) is employed to identify key features for predicting coarsening behaviors of γ' phases in Co/CoNi-based superalloys. SBS initiates with the full set of $N$ features and sequentially removes the least important features until reaching the minimum of a loss function, yielding a subset of $n$ selected features.

Additionally, the t-distributed stochastic neighbor embedding (t-SNE) technique[41] is utilized to visually assess the impact of feature selection on the dataset, both before and after applying SBS. This visualization aids in understanding the data structure and evaluating the effect of feature selection.

**Model evaluation**
The performances of classification were evaluated using accuracy, which is defined by

$$Accuracy = \frac{N_c}{N_c + N_w} \tag{7}$$

where $N_c$ and $N_w$ represent the number of correctly and wrongly classified samples, respectively. In this study, a ten-fold cross-validation method was employed to avoid overfitting. This entailed the random division of the training dataset into ten folds, with nine used for model training and the remaining serving as the validation fold. This process was repeated ten times, with each fold acting as the validation set once. The cross-validation performance was obtained by averaging the ten validation performances.

## RESULTS AND DISCUSSION
**Classification models based on CP features**
An XGBoost classifier (XGBC) model with default hyperparameters was employed to predict $K_{cla}$ of Co/CoNi-based superalloys. The SBS was wrapped with the XGBC to identify an optimal combination of features. Figure 1A shows the cross-validation accuracy (CV-Accuracy) of the XGBC model as a function of the number of SBS-selected features, using CP as input features. The CV-Accuracy of the XGBC model increases with the number of SBS-selected features, peaking at 0.924 with four features. Beyond this point, the CV-Accuracy remains constant with up to eight features and then declines rapidly. The four features ultimately selected are the $T$, and the atomic fraction of Ti, V, and Ta elements. Figure 1B and C shows the t-SNE representations of the data before and after SBS feature selection, respectively. The t-SNE plots demonstrate that the SBS-selected features effectively enhance the separation between the two categories,
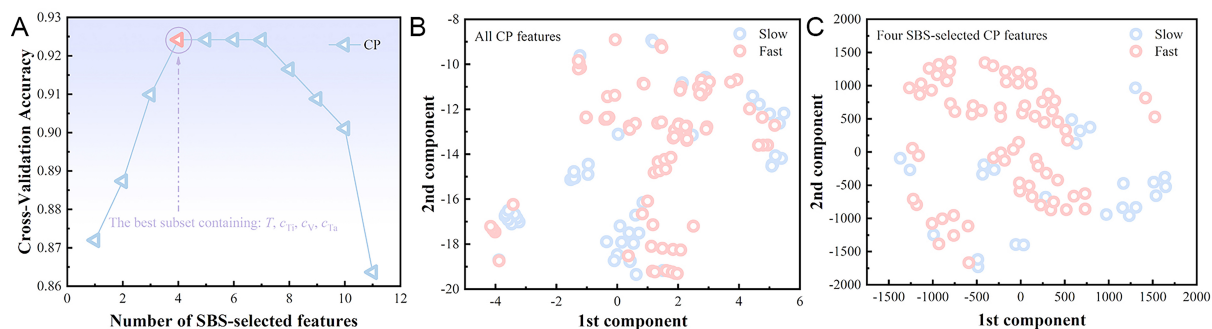
**Figure 1.** (A) Cross-validated accuracy of XGBC model using the CP features selected by SBS approach. The t-SNE representation of data: (B) All CP features, (C) Four SBS-selected CP features. XGBC: XGBoost classifier; CP: constituent elements and processing parameters; SBS: sequential backward selector; t-SNE: t-distributed stochastic neighbor embedding.

indicating improved classification distinguishability. The detailed classification results are displayed in the Supplementary Figure 2.

### Model interpretation based on SHAP value

To explore the "black box" nature of the XGBC model, a game theory-based approach, SHAP, was employed to analyze constructed ML model. This method examines the contribution of each feature in the trained XGBC model to the predictions of $K_{cla}$, referred to as SHAP values[18]. In binary classifications, the SHAP algorithm identifies attributes characteristic of the positive class. Given that the Slow coarsening category is associated with a positive value, a positive SHAP value for a feature indicates that the feature slows down the coarsen of ' phase, while a negative SHAP value suggests an accelerating coarsen effect.

Figure 2A ranks the mean absolute SHAP values of four SBS-selected CP features for $K_{cla}$, while Figure 2B-E illustrates the SHAP values for individual data points in the dataset. A pivotal finding from this analysis is the identification of a distinct threshold that segregates SHAP values into positive and negative regions. Notably, the mean absolute SHAP values for $T$ significantly surpass those of other features, underscoring the service temperature as a critical factor influencing the coarsening behavior of Co/CoNi-based superalloys. SHAP values transition to negative when $T$ exceeds 900 °C, correlating with an increased $K_r$ for the γ' phase. This suggests that most existing Co-based superalloys undergo pronounced coarsening when operating above this temperature[42]. Additionally, SHAP values shift to negative when the atomic fraction of the Ti element ($c_{Ti}$) exceeds 0.025, the atomic fraction of the V element ($c_V$) exceeds 0.04, and the atomic fraction of the Ta element ($c_{Ta}$) exceeds 0.02. A substantial body of literature identifies both coarsening-promoting and coarsening-limiting elements. However, there is no consensus on the optimal composition range. Mukhopadhyay *et al.* reported an increase in the γ' coarsening rate at 900 and 950 °C, peaking for alloys with the highest Ti content[13]. Qu *et al.* reveal that the $K_r$ of the γ' precipitate is strongly dependent on the $T$, and it increases nearly ten times with the $T$ rising from 800 to 900 °C[43]. Within this temperature range, the activation energy for coarsening of the γ' precipitates is estimated to be 230 kJ/mol, which is close to the activation energy for the diffusion of V in Co. This suggests that the coarsening rate of γ' precipitates is limited by the diffusion of V.

These insights are significant for designing Co/CoNi-based superalloys that resist γ' phase coarsening. They also identify a range of characteristics for the key factors influencing coarsening, which are crucial for optimizing the material properties of these alloys.
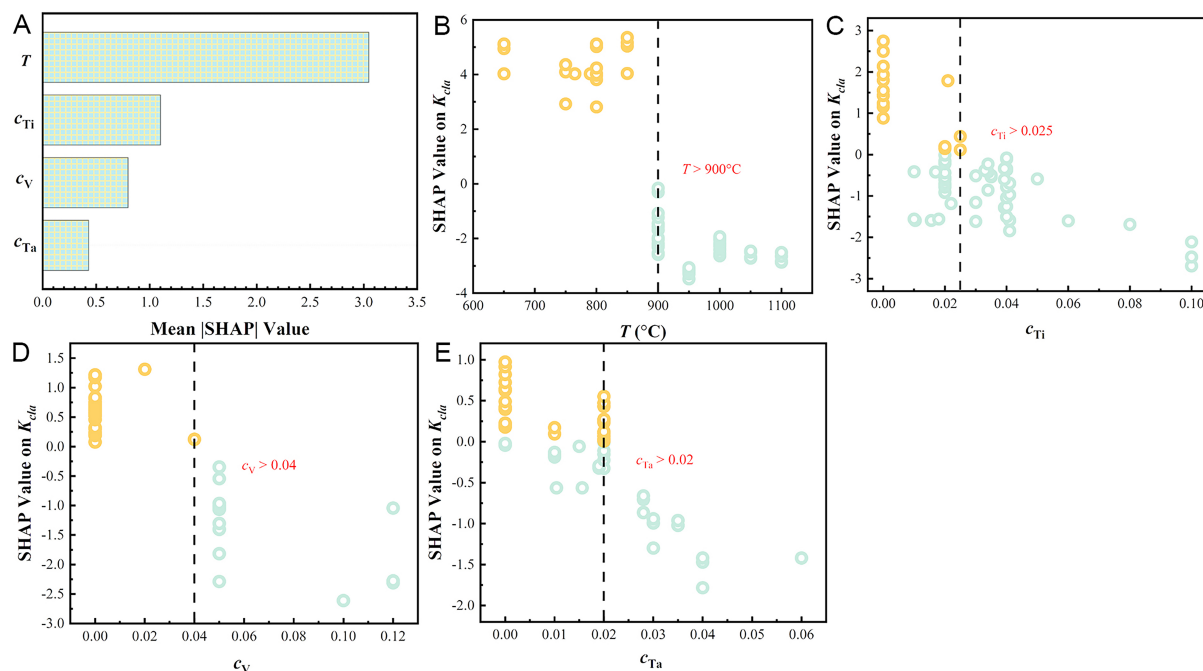
**Figure 2.** (A) Ranked mean absolute value of SHAP values of four SBS-selected CP features using XGBC model for $K_{cla}$. The SHAP values (negative in cyan, positive in orange) of (B) $T$, (C) $c_{Ti}$, (D) $c_V$, and (E) $c_{Ta}$ for every one of the data. XGBC: XGBoost classifier; CP: constituent elements and processing parameters; SHAP: SHapley Additive exPlanation.

## Accuracy improvement with general CPAE features

However, additional alloying elements beyond Ti, V, and Ta, such as Ni, Al, and Mo, which are strong γ' phase forming elements, also affect the coarsening behavior of Co/CoNi-based superalloys. Therefore, more general CPAE features were employed here to predict the coarsening behaviors. Similarly, the SBS algorithm was wrapped with XGBC to select the optimal subset of CPAE features. As shown in Figure 3A, when using CPAE as the input features, the CV-Accuracy similarly increases with the number of SBS-selected features, reaching a maximum of 0.932 with seven features, indicating a slightly superior performance compared to using CP alone. This suggests that atomic and electronic properties significantly influence the coarsening behavior of γ' phases.

The seven features finally chosen for CPAE are $T$, $E$, $EN$, $r$, $c_{Ti}$, the differences of atomic radius ($\sigma r$), and the differences of electronegativity ($\sigma EN$), respectively. The common features of both CP and CPAE feature sets are $T$ and $c_{Ti}$, indicating that the $T$ and Ti content significantly influence the coarsening behavior of γ' phases. Figure 3B-C depicts t-SNE representation of the data before and after SBS of CPAE features. Notably, the seven CPAE features can more effectively differentiate between the two categories than the CP features, further indicating the efficiency of introducing general atomic and electronic properties. This enhancement also can be visually corroborated by the confusion matrix depicted in Supplementary Figure 3A. With this enriched feature set, the $F_1$ scores [defined in Equation (S3) of the Supplementary Materials] for the Slow and Fast categories increased to 0.905 and 0.947, respectively. Supplementary Figure 3B showcases the receiver operating characteristic (ROC) curve for the Slow category using this screening feature set, where the area under the curve (AUC) has risen to 0.946, highlighting the significant impact of integrating atomic and electronic features on model performance.
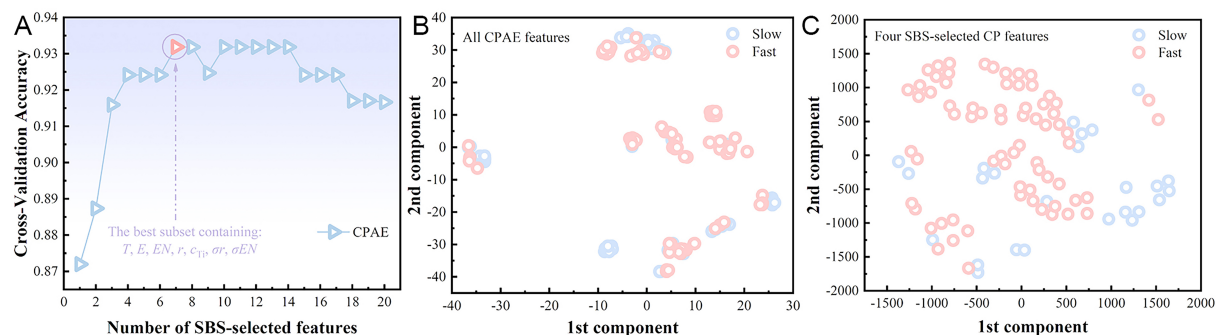
**Figure 3.** (A) Cross-validated accuracy of XGBC model applied to the CPAE features selected by SBS approach. The t-SNE representation of data: (B) All CPAE features, (C) Seven SBS-selected CPAE features. XGBC: XGBoost classifier; CPAE: constituent elements, processing parameters, and atomic and electronic properties; SBS: sequential backward selector; t-SNE: t-distributed stochastic neighbor embedding.

Additionally, Figure 4A ranks the mean absolute SHAP values of the seven SBS-selected CPAE features for $K_{cla}$, with $T$ and $E$ displaying notably higher values than other features. Figure 4B-H plots the SHAP values for each data point in general features dataset. Similar to CP features, a critical threshold exists for most CPAE features, dividing SHAP values into positive and negative domains. Specifically, the SHAP values are positive when $T$ is below 900 °C, $E$ exceeds 195.95 GPa, $c_{Ti}$ is less than 0.01, $\sigma r$ remains under 15.396 pm, and $\sigma EN$ stays below 0.12, indicating that the γ' phase exhibits slow coarsening behavior under these conditions. Liu *et al*. demonstrated that elements with a high $E$ (e.g., Re, Ru, W, and Mo) tend to enter the γ phase or be distributed relatively uniformly within the γ/γ' phases, resulting in increased lattice constants for both phases[14,15]. The simultaneous enlargement of the γ and γ' phases reduces the mismatch between them, thereby alleviating the elastic stress at their interface. This ultimately leads to the formation of new Co-based superalloys with relatively small γ' phase sizes. While these results align with our findings, we provided specific ranges of $E$ as shown in Figure 4C. Figure 4G demonstrates that a smaller deviation in atomic radii correlates with a lower coarsening rate. When the atomic radii of different elements in the alloy are more similar, this enhanced uniformity can mitigate the local stresses induced by atomic size mismatches. This reduction in local stresses may subsequently slow the migration velocity of phase boundaries, leading to a decreased rate of coarsening[44]. Furthermore, Figure 4H illustrates that a smaller deviation in $EN$ is linked to a lower rate of coarsening. A low standard deviation of $EN$ indicates that the electronegativities of the elements in the alloy are similar, which typically implies more cohesive chemical interactions and minimal differences in electron affinity. Such a chemical environment may result in more uniform interatomic interaction forces within the alloy, thereby reducing local chemical inhomogeneity. During the coarsening process of superalloy, the coarsening rate of $L1_2$ phases is related to the chemical inhomogeneity within the alloy and the stability of its microstructure. If the $EN$ differences are minimal, the γ/γ' phase interfaces in the alloy are more stable and exhibit a reduced tendency to diffuse into each other, thereby decreasing the coarsening rate of the γ' phase[44].

**Analytic formula to predict coarsening behavior of γ' phase**

The features selected by SBS for CP and CPAE are combined using basic mathematical operators. These combined features are then subjected to SC, which aims to derive a mathematical formula for $K_{cla}$. SC typically employs genetic programming (GP) to identify formulas from a pool of candidate expressions (individuals). Beginning with an initial population of random candidates, SC evaluates all individuals and identifies the most promising ones. Subsequent generations are formed from new individuals created through evolutionary operators, including crossover and mutation. This iterative process ensures that the
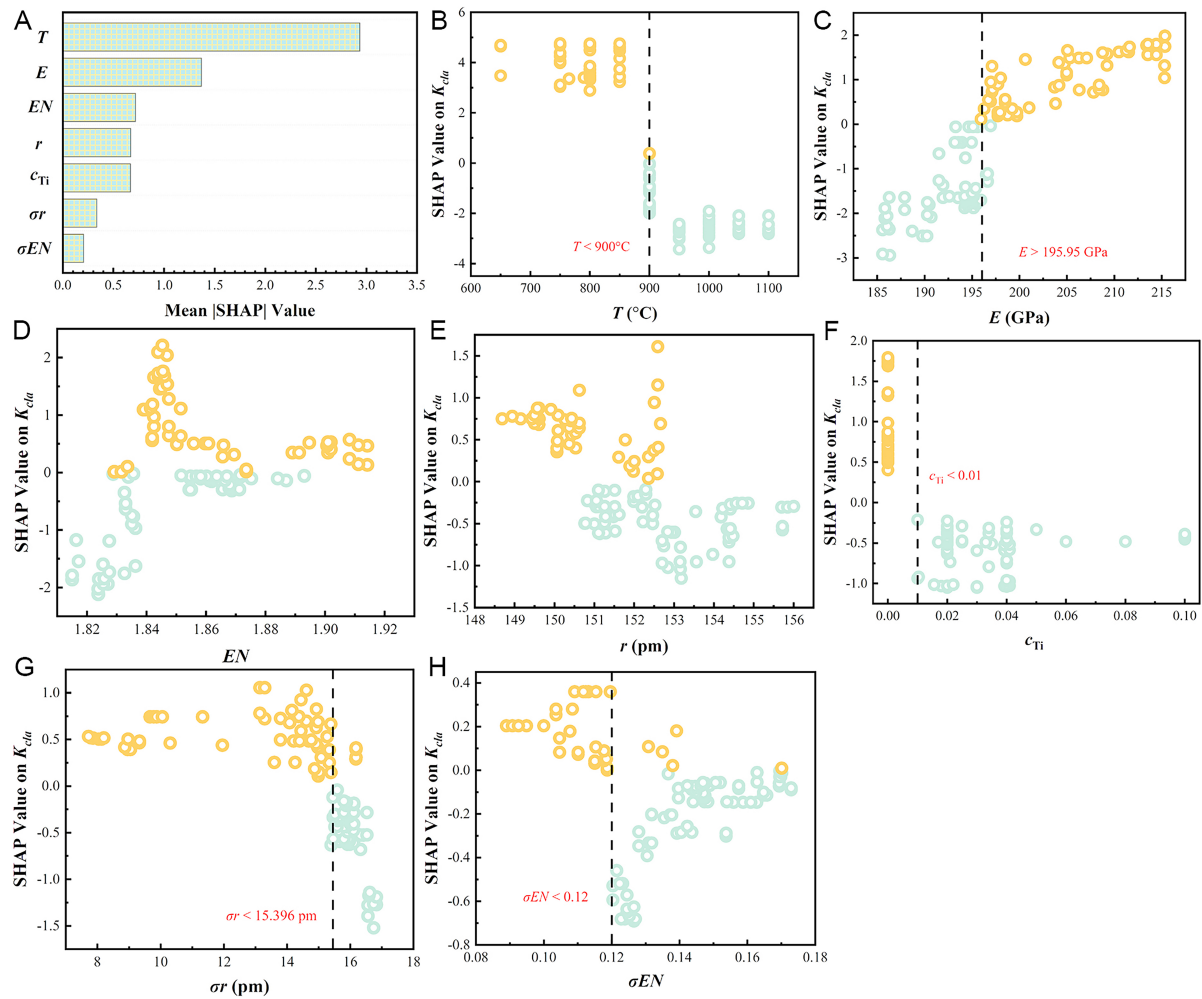
**Figure 4.** (A) Ranked mean absolute value of SHAP values of seven SBS-selected CPAE features using XGBC model for $K_{cla}$. The SHAP values (negative in cyan, positive in orange) of (B) $T$, (C) $E$, (D) $EN$, (E) $r$, (F) $c_{Ti}$, (G) $\sigma r$, and (H) $\sigma EN$ for every one of the data. SHAP: Shapley Additive Explanation; SBS: sequential backward selector; CPAE: constituent elements, processing parameters, and atomic and electronic properties; XGBC: XGBoost classifier.

most effective individuals are retained, culminating in the selection of the optimal analytic formula for predicting $K_{cla}$.

Utilizing the four SBS-selected CP features and basic mathematic operators (addition, subtraction, multiplication, and division), the SC performs 1,000 iterations. Each iteration involves 5,000 individuals, each represented as an expression tree, with constants, features, and mathematic operators as nodes. The depth of the trees is constrained to a maximum of 10 to limit model complexity and avoid overfitting. Twenty independent GP runs were conducted, yielding Equation (8), which exhibited the highest accuracy of 0.871 from a pool of 100 million individuals. Analysis of the formula reveals that $T$, $c_{Ti}$ and $c_{Ta}$ are negatively correlated with coarsening behavior of γ' phases, aligning with findings from previous analysis using SHAP. Furthermore, the component concerning $T$ in Equation (8), which shares a similar expression form with the theoretical formula $K_r$ [as given in Equation (3)], is represented as $1/T$, underscoring the validity of utilizing the SC algorithm. Figure 5 illustrates the demarcation line between the Slow and Fast categories, with a threshold $K_{cla}$ of 0.369, effectively distinguishing the two classifications and demonstrating the strong predictive capability of Equation (8).
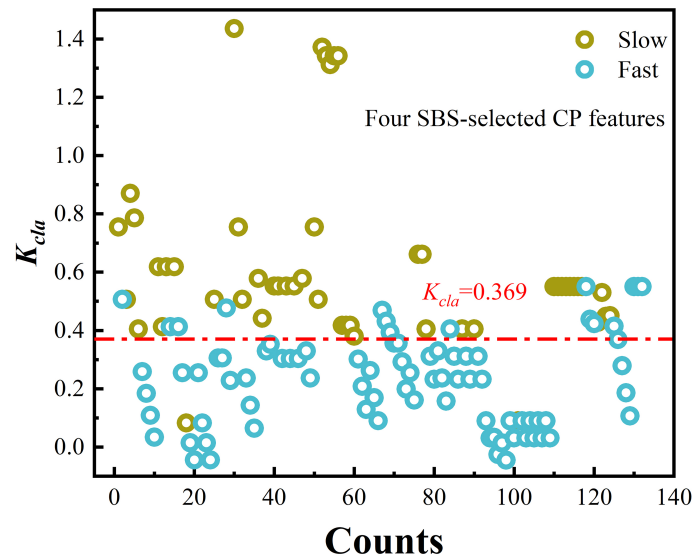
**Figure 5.** Visualization of demarcation line between the Slow and Fast coarsening categories utilizing four SBS-selected CP features. SBS: Sequential backward selector; CP: constituent elements and processing parameters.

$$K_{cla} = -5.0704c_{Ta} - 3.7509c_{Ti} + \frac{1}{0.0016084T - 0.55879} - 0.61897 \tag{8}$$

Similarly, the process was replicated using seven SBS-selected CPAE features and the same basic mathematical operators, again undergoing 1,000 iterations. Each iteration involved 5,000 individuals represented as expression trees, and the tree depth was likewise limited to 10. From twenty independent GP runs, Equation (9) was identified, achieving the highest accuracy of 0.9167 from 100 million individuals. As indicated by the formula, $T$, $c_{Ti}$ and $\sigma r$ are negatively correlated with the coarsening behavior of the $\gamma'$ phase, consistent with previous SHAP analysis results. Conversely, $E$ exhibits a positive correlation with the coarsening behavior, corroborating earlier findings. The component concerning $T$ in Equation (9), which also mirrors the theoretical formula $K_r$ (as given in Equation (3)), is expressed as $1/T$, further supporting the appropriateness of employing the SC algorithm. Figure 6 presents the demarcation line between the Slow and Fast categories, with a threshold $K_{cla}$ of 0.322, clearly distinguishing the classifications and highlighting the predictive power of Equation (9).

$$K_{cla} = -0.033586\sigma r - 2.783c_{Ti} + \frac{0.091674E}{0.046906T - 20.986} \tag{9}$$

Our previous analysis indicates that Equation (9) demonstrates superior accuracy compared to Equation (8). Table 1 outlines the misclassified experimental samples for both formulas. Among the 132 experimental samples in the original dataset, Equation (8) misclassified 17 samples, whereas Equation (9) misclassified only 7. Notably, of the 17 samples misclassified by Equation (8), Equation (9) correctly classified 11. Upon examining these 11 samples, it was observed that when relying solely on the CP feature, certain alloy samples either lacked Ti, Ta, and V elements or contained only one or two of these elements in relatively low amounts. Moreover, the $K_r$ values were situated at the boundary between the Slow and Fast categories, elucidating why reliance solely on the CP feature resulted in classification errors. Further analysis revealed that of the seven samples misclassified by Equation (9), six were also incorrectly classified by Equation (8). Both formulas incorporate the feature variables $T$ and $c_{Ti}$. A detailed examination of these six experimental samples indicated that a sample with $T$ of 1,000 °C and relatively high Ti content was classified into the Slow category, an unexpected outcome that contradicts prior assumptions. A review of the original dataset and

**Table 1. Experiment samples misclassified by Equations (8) and (9)**

| Counts | $c_{Ta}$ | $c_{Ti}$ | $c_V$ | $T$ (°C) | $E$ (GPa) | EN | $\sigma EN$ | $r$ (nm) | $\sigma r$ | $K_r$ (nm$n$/s) | Equation (8) | Equation (9) |
|---|---|---|---|---|---|---|---|---|---|---|---|---|
| | | | | | | | | | | CP and CPAE features | | |
| 2 | 0 | 0 | 0 | 900 | 215.3 | 1.90 | 0.17 | 153 | 16.8 | 2.65 | × | × |
| 12 | 0 | 0 | 0 | 950 | 215.3 | 1.90 | 0.17 | 153 | 16.5 | 0.92 | √ | × |
| 14 | 0 | 0 | 0 | 950 | 214.4 | 1.91 | 0.17 | 152 | 16.6 | 1.65 | × | √ |
| 16 | 0 | 0 | 0 | 950 | 213.5 | 1.91 | 0.17 | 152 | 16.6 | 2.15 | × | √ |
| 18 | 0.02 | 0.04 | 0 | 1,000 | 209.2 | 1.87 | 0.17 | 154 | 16.2 | 0.48 | × | × |
| 28 | 0.04 | 0.02 | 0.05 | 1,000 | 185.6 | 1.83 | 0.13 | 151 | 15.5 | 3.63 | × | × |
| 67 | 0 | 0.01 | 0 | 900 | 195.4 | 1.87 | 0.12 | 151 | 15.4 | 2.96 | × | √ |
| 68 | 0 | 0.02 | 0 | 900 | 194.5 | 1.86 | 0.12 | 151 | 15.6 | 21.62 | × | √ |
| 69 | 0 | 0.03 | 0 | 900 | 193.5 | 1.86 | 0.13 | 151 | 15.8 | 25.23 | × | √ |
| 84 | 0.02 | 0 | 0.05 | 900 | 185.8 | 1.84 | 0.12 | 151 | 14.9 | 1.24 | × | √ |
| 101 | 0.02 | 0.02 | 0 | 1,050 | 197.0 | 1.85 | 0.14 | 151 | 15.4 | 0.53 | × | √ |
| 118 | 0 | 0.1 | 0.04 | 750 | 186.3 | 1.83 | 0.13 | 153 | 12.0 | 6.83 | × | √ |
| 119 | 0 | 0.018 | 0 | 900 | 196.5 | 1.86 | 0.12 | 152 | 15.6 | 1.77 | × | √ |
| 120 | 0 | 0.022 | 0 | 900 | 198.8 | 1.85 | 0.13 | 152 | 15.9 | 2.36 | × | √ |
| 125 | 0.0104 | 0.0104 | 0 | 900 | 203.7 | 1.87 | 0.15 | 152 | 16.3 | 7.33 | × | √ |
| 130 | 0 | 0.1 | 0.1 | 750 | 190.7 | 1.82 | 0.12 | 156 | 8.9 | 2.54 | × | × |
| 131 | 0 | 0.1 | 0.1 | 750 | 190.3 | 1.83 | 0.12 | 156 | 9.0 | 1.85 | × | × |
| 132 | 0 | 0.1 | 0.1 | 750 | 189.8 | 1.83 | 0.12 | 156 | 9.0 | 1.27 | × | × |

CP: Constituent elements and processing parameters; CPAE: constituent elements, processing parameters, and atomic and electronic properties.

relevant literature revealed that this sample exhibited $n$ of 2.24, indicative of a competitive interaction between the LSW and TIDC mechanism, thereby rationalizing the observed smaller $K_r$ values. Moreover, at a lower $T$ of 750 °C with reduced Ti content, the samples were classified into the Fast category. The $K_r$ values situated at the boundary between the Slow and Fast categories further elucidate the classification results. In light of these contentious samples, we recommend conducting additional experimental investigations to corroborate these findings and to incorporate new experimental data into our dataset to enhance model accuracy. Currently, Equation (9) achieves an accuracy exceeding 0.9, affirming its robust classification capability. To further validate the model's effectiveness, we conducted comparative tests using alloy samples available within our research group.
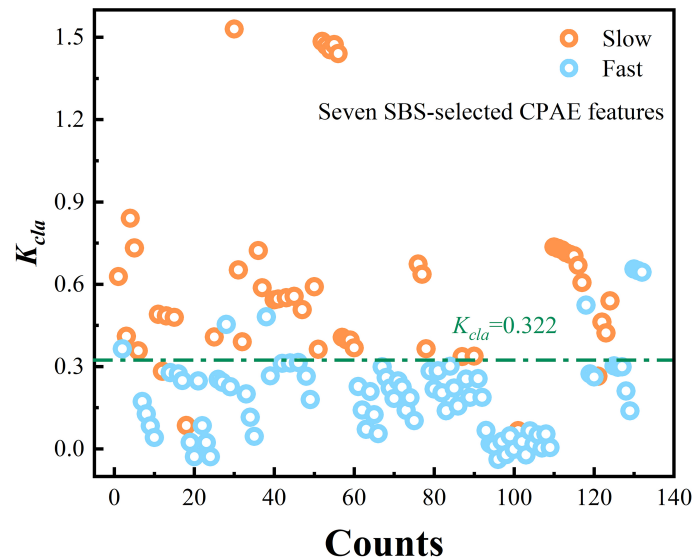
**Figure 6.** Visualization of demarcation line between the Slow and Fast coarsening categories utilizing seven SBS-selected CPAE features. SBS: Sequential backward selector; CPAE: constituent elements, processing parameters, and atomic and electronic properties.

## Valid verification of analytic formula

To validate the reliability of Equation (9), derived from the SC algorithm, three candidate alloys with specific atomic percentages were selected for experimental characterization. These alloys are designed as follows: Co-30Ni-7.5Al-2.5Ti-2Cr, Co-30Ni-7.5Al-2.5Ti-2Mo, Co-35Ni-9Al-6Ti-4Cr-3Ta-1Mo, designated as 2Cr, 2Mo, and 6Ti4Cr3Ta1Mo, respectively. The first two alloys, 2Cr and 2Mo, have been extensively characterized by our prior works, as reported in references[45-48]. Notably, the γ' phase solvus temperatures of both alloys have been confirmed to be below 900 °C, according to reference[48]. Given the relatively low γ' phase solvus temperature, we proceeded to investigate the coarsening evolution of the γ' phases through isothermal aging at 750 °C for durations of 16, 32, 6, and 128 h, followed by air cooling.

To synthesize the third alloy, raw metals with a minimum purity level of 99.95 % were melted at least eight times in a vacuum arc-melting furnace, yielding ingots weighing 50 g. The measured composition of the ingot, as determined by an X-ray fluorescence spectrometer (XRF), is provided in Table 2. Subsequently, the ingot specimens underwent solution treatment at 1,280 °C for 24 h in a vacuum tube furnace, followed by furnace cooling. They were then aged at 900, 950, 1,000, and 1,050 °C for durations of 25, 10, 200, and 400 h, respectively, to study the microstructural evolution of coherent γ/γ' phases, followed by air cooling.

The microstructure of each candidate alloy was characterized using a field emission scanning electron microscope (ZEISS SUPPA 55). Prior to the scanning electron microscopy (SEM) analysis, all candidate alloys were prepared according to standard metallographic procedures and electrolytically etched for several seconds using a solution with an $H_3PO_4$ to $H_2O$ ratio of 1:5. The micrographs obtained from the SEM were converted to binary images using a combination of manual and automatic coloring techniques via the Image Pro Plus software package. The mean sizes of the precipitates were quantified using the Image Pro Plus particle analysis tool, identical to the previous data processing procedure. To ensure statistical reliability, three to five images were analyzed for each alloy. Subsequently, regression analysis of the experimental coarsening data was performed using the OriginPro software package.

**Table 2. Nominal and measured composition of the third candidate alloys (at.%)**

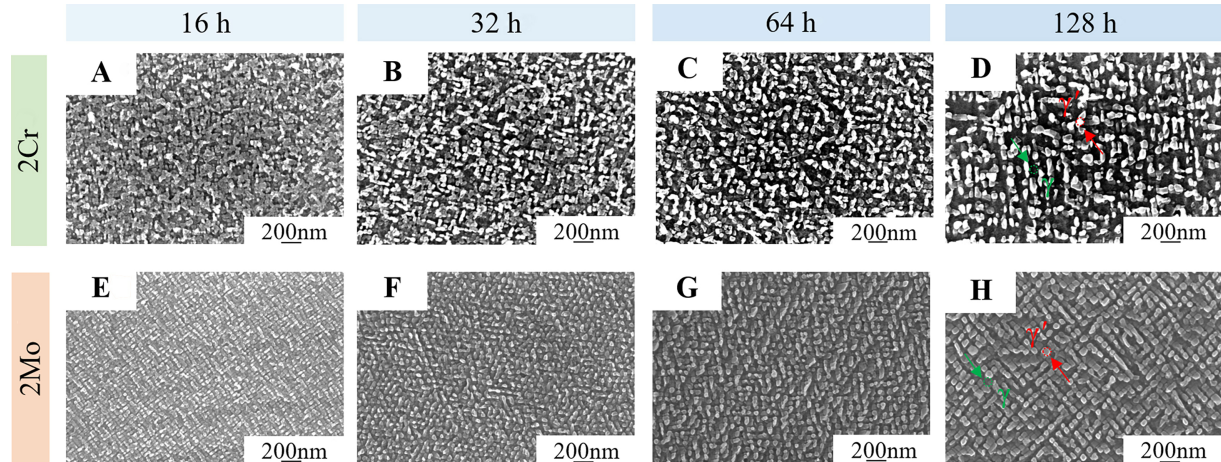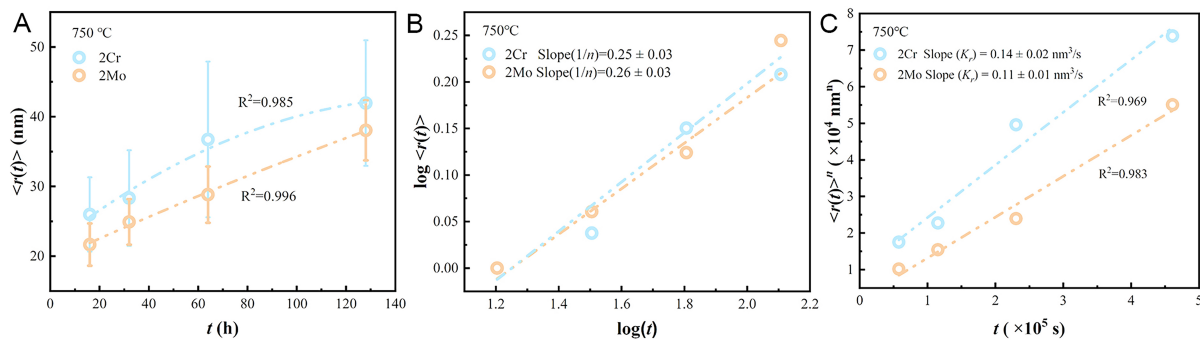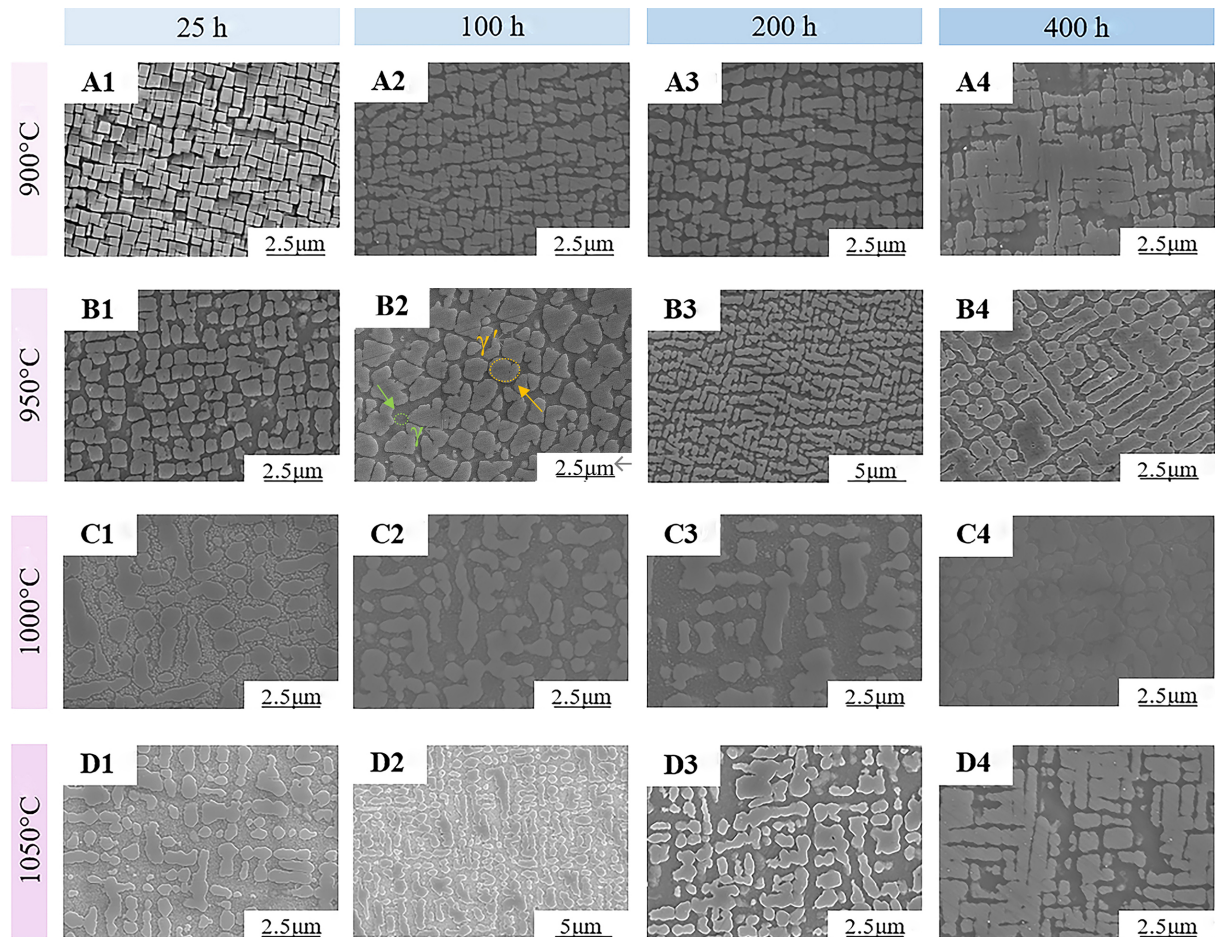|          | Co   | Ni   | Al  | Ti  | Cr  | Ta  | Mo  |
|----------|------|------|-----|-----|-----|-----|-----|
| Nominal  | Bal. | 35.0 | 9.0 | 6.0 | 4.0 | 3.0 | 1.0 |
| Measured | Bal. | 36.5 | 9.1 | 6.0 | 3.9 | 2.8 | 1.0 |



**Figure 7.** Typical γ/γ' microstructures (green color arrow represents γ phase; red color arrow represents γ' phase), of alloy 2Cr and 2Mo after aging at 750 °C for (A and E):16 h, (B and F): 32 h, (C and G): 64 h, (D and H): 128 h, respectively.



**Figure 8.** (A) Plot showing average equivalent radius $r$ of the γ' precipitate versus aging time $t$ during isothermal aging at 750 °C in the 2Cr and 2Mo alloys; (B) Plot between $\log{<}r(t){>}$ vs. $\log(t)$ in the designed 2Cr and 2Mo alloys during isothermal aging at 750 °C giving the temporal growth exponent of γ' phases, which corresponds to classical LSW growth exponent; (C) Variation of the average equivalent radius $r(t)^3$ of γ' phases with the aging time $t$ in the 2Cr and 2Mo alloys where the linear fitting curves are shown, and the fitted slopes corresponding to coarsening rate constant $K_r$; the coefficient of determination $R^2$ is also marked.

Figure 7 depicts the typical microstructures of the 2Cr and 2Mo alloys after aging at 750 °C for periods ranging from 16 to 128 h. Both alloys exhibit a consistent γ/γ' two-phase microstructure, devoid of any secondary phase precipitation. In the 2Cr alloy, as shown in Figure 8A, the mean radius of the γ' phases was measured at 25.99 ± 5.33 nm, 28.34 ± 6.85 nm, 36.74 ± 11.16 nm, 41.96 ± 9 nm corresponding to aging durations of 16, 32, 64, and 128 h, respectively. Correspondingly, the mean radius of the γ' phases in the 2Mo alloy was 21.67 ± 3.02 nm, 24.92 ± 3.26 nm, 28.83 ± 4.04 nm, 38.05 ± 4.31 nm for the same aging periods. Figure 8B plots the logarithm of average precipitate radius $\log r(t)$ against the logarithm of the aging time $\log t$ for both alloys, where multiple linear regression analysis of the data yields inverse temporal exponents ($1/n$) of 0.25 ± 0.03 for the 2Cr alloy and 0.26 ± 0.03 for the 2Mo alloy at 750 °C. These values are in close proximity to the predicted value of 0.33 from the LSW model, indicating that LSW theory may

**Figure 9.** Typical γ/γ' microstructures (light green color arrow represents γ phase; orange color arrow represents γ' phase) of the 6Ti4Cr3Ta1Mo alloy after aging in the temperature range from 900 to 1,050 °C for different durations from 25 to 400 h. (A) 900 °C; (B) 950 °C; (C) 1,000 °C; (D) 1,050 °C. 1: 25 h; 2: 100 h; 3: 200 h; 4: 400 h.

adequately describe the coarsening kinetics observed in the studied alloy. However, further data points are necessary to achieve a comprehensive understanding of the coarsening mechanism. Figure 8C illustrates the correlation between the average precipitate radius $r(t)^3$ and aging time $t$ during isothermal aging at 750 °C for the 2Cr and 2Mo alloys, respectively. The derived $K_r$ is approximately $0.14 ± 0.02$ nm³/s for the 2Cr alloys and $0.11 ± 0.01$ nm³/s for 2Mo alloys. Both values are below 1 nm³/s, classifying them as Slow coarsening category.

The $K_{cla}$ values for both alloys were calculated using Equations (4), (5), and (9). Equation (9) elucidates that $K_{cla}$ is influenced by $T$, $c_{Ti}$, $E$ and the standard deviation of $r$ of the elements constituting the γ' phases in Co/CoNi-based superalloy, as detailed in Table 3. The calculations yield $K_{cla}$ values of 0.852 and 0.816 for the 2Cr and 2Mo alloys, respectively. As illustrated in Figure 6, the demarcation line for Slow and Fast coarsening categories is set at a threshold of 0.322, with values exceeding this threshold classified as Slow coarsening categories. Consequently, both alloys fall within the Slow coarsening category range, aligning with the experimental outcomes.

Figure 9 portrays typical γ/γ' microstructures of the 6Ti4Cr3Ta1Mo alloy aged at 90, 950, 1,000 and 1,050 °C over durations from 25 to 400 h. The respective mean radius of the γ' phase is shown in Figure 10A.

**Table 3. Young's modulus $E$ and atomic radius $r$ of the elements constituting the $\gamma'$ phases in Co/CoNi-based superalloy**

|  | Co | Ni | Al | Ti | Cr | Ta | Mo |
|---|---|---|---|---|---|---|---|
| $E$ (GPa)[a] | 209 | 200 | 70 | 116 | 279 | 186 | 329 |
| $r$ (nm)[b] | 152 | 149 | 118 | 176 | 166 | 200 | 190 |
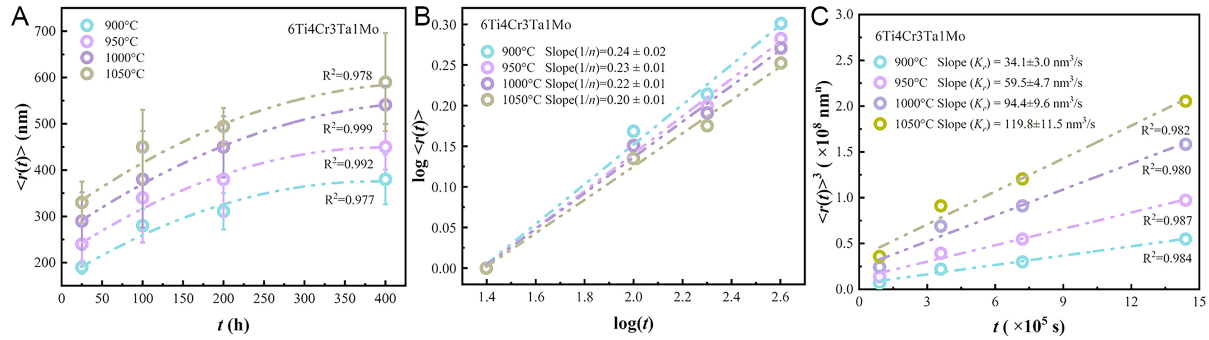


**Figure 10.** (A) Plot showing average equivalent radius $r$ of the $\gamma'$ precipitate *vs.* aging time $t$ during isothermal aging at 900, 950, 1,000, and 1,050 °C in the 6Ti4Cr3Ta1Mo alloy; (B) Plot between $\log< r(t) >$ *vs.* $\log(t)$ for the 6Ti4Cr3Ta1Mo alloy during isothermal aging at 900, 950, 1,000, and 1,050 °C giving the temporal growth exponent of $\gamma'$ phases, which corresponds to classical LSW growth exponent; (C) Variation of the average equivalent radius $r(t)^3$ of $\gamma'$ phases with the aging time $t$ in the 6Ti4Cr3Ta1Mo alloy where the linear fitting curves are shown, and the fitted slopes corresponding to coarsening rate constant $K_r$, as well as the coefficient of determination $R^2$ are also marked.

Figure 10B plots the logarithm of average precipitate radius $\log r(t)$ against the logarithm of the aging time $\log t$ for this alloy, where multiple linear regression analysis yields inverse temporal exponents ($1/n$) of 0.24 ± 0.02, 0.23 ± 0.01, 0.22 ± 0.01, and 0.20 ± 0.01 at 900, 950, 1,000 and 1,050 °C, respectively. These values suggest the LSW model may adequately describe the coarsening kinetics at these temperatures; however, additional data would enhance understanding. Figure 10C illustrates the correlation between the average precipitate radius $r(t)^3$ and aging time $t$, with derived $K_r$ markedly higher at 34.1 ± 3.0 nm³/s, 59.5 ± 4.7 nm³/s, 94.4 ± 9.6 nm³/s, 119.8 ± 11.5 nm³/s for the respective temperatures. All values exceed 1 nm³/s, indicating a Fast coarsening category classification.

The $K_{cla}$ of the 6Ti4Cr3Ta1Mo alloy was calculated at varying $T$ using the formulas provided in Equations (4), (5) and (9). The $K_{cla}$ values at temperatures of 900, 950, 1,000 and 1,050 °C are 0.15, 0.06, -0.004, and -0.06, respectively. As depicted in Figure 6, the $K_{cla}$ is classified as Slow coarsening category for values above 0.322, and as Fast coarsening category for values below this threshold. Consequently, all four $T$ values fall within the Fast coarsening category range, which is consistent with the experimental findings.

## CONCLUSIONS

This study presents an XGBC model for predicting the coarsening behavior of $\gamma'$ phase in Co/CoNi-based superalloys. A dataset comprising 132 samples was constructed, which includes 11 features related to CP and 20 features that encompass CPAE. The adopted feature selection method identified four CP features: $T$, $c_{Ti}$, $c_V$, and $c_{Ta}$, and seven CPAE features: $T$, $E$, $EN$, $r$, $c_{Ti}$, $\sigma r$, and $\sigma EN$, respectively.

The SHAP analysis, employing the identified CP and CPAE features, revealed a threshold for the majority of these features. This critical feature value delineates the SHAP values into positive and negative regions. Consequently, feature values in the positive SHAP value region enhance the coarsening behavior of the $\gamma'$ phase, while those in the negative region impede it. This distinction provides a clear basis for designing Co/

CoNi-based superalloys with reduced coarsening rate. Furthermore, the study provided explicit mathematical expressions for predicting $K_{cla}$ and utilized three candidate alloys to validate the accuracy of the optimal formula. The results demonstrated good agreement between the experimental outcomes and computational predictions, thereby offering valuable insights for the expeditious design of novel anti-coarsening Co/CoNi-based superalloys.

## DECLARATIONS

### Acknowledgements

### Authors' contributions

Data acquisition, data analysis, and manuscript drafting: Sun L
Project conceptualization, investigation, methodology, analyzed data, and manuscript revision: Xiong J
Project conceptualization, methodology, supervision, manuscript revision, and funding acquisition: Gao Q
Discussion of the results: Sun L, Ma Q, Zhang J, Yu L, Xiong J, Li H, Gao Q

### Availability of data and materials

Data sources in the study are provided in the Supplementary Materials.

### Financial support and sponsorship

### Conflicts of interest

All authors declare that there are no conflicts of interest.

### Ethical approval and consent to participate

Not applicable.

### Consent for publication

Not applicable.

### Copyright

## REFERENCES

1.  Sato J, Omori T, Oikawa K, Ohnuma I, Kainuma R, Ishida K. Cobalt-base high-temperature alloys. *Science* 2006;312:90-1. DOI PubMed
2.  Zhuang X, Antonov S, Li L, Feng Q. γ'-strengthened multicomponent CoNi-based wrought superalloys with improved comprehensive properties. *Metall Mater Trans A* 2023;54:1671-82. DOI
3.  Bauer A, Neumeier S, Pyczak F, Göken M. Microstructure and creep strength of different γ/γ'-strengthened Co-base superalloy variants. *Scripta Materialia* 2010;63:1197-200. DOI
4.  Neumeier S, Freund LP, Bezold A, et al. Advanced polycrystalline γ'-strengthened CoNiCr-based superalloys. *Metall Mater Trans A* 2024;55:1319-37. DOI
5.  Li J, Zhang J, Li Z, et al. Effect of Ti/Nb/Ta addition on the γ/γ' coherent microstructure in low-density and high-strength Co-Al-W-

Mo-based superalloys. *J Mater Sci Technol* 2024;186:174-87.  DOI

6.   Wang C, Zhuo H, Zheng D, et al. Development of a low-density Co-Ni-Al-Ta-Cr superalloy with high mechanical performance and superior oxidation resistance. *Mater Des* 2024;238:112673.  DOI

7.   Sun L, Cao B, Ma Q, et al. Machine learning-assisted composition design of W-free Co-based superalloys with high γ'-solvus temperature and low density. *J Mater Res Technol* 2024;29:656-67.  DOI

8.   Yang Z, Liu X, Zhao J, et al. Discontinuous coarsening leads to unchanged tensile properties in high-entropy alloys with different recrystallization volume fractions. *Int J Plast* 2024;176:103963.  DOI

9.   Lin M, Lu J, Chen Y, et al. 800°C-stable D0$_{22}$ superlattice in a NiCrFe-based medium entropy alloy. *Mater Res Lett* 2024;12:172-9.  DOI

10.  He F, Chen D, Han B, et al. Design of D0$_{22}$ superlattice with superior strengthening effect in high entropy alloys. *Acta Mater* 2019;167:275-86.  DOI

11.  Li X, Ma Q, Liu E, et al. Order phase transition of HIP nickel-based powder superalloy during isothermal aging. *J Alloys Compd* 2025;1010:177269.  DOI

12.  He F, Zhang K, Yeli G, et al. Anomalous effect of lattice misfit on the coarsening behavior of multicomponent L1$_2$ phase. *Scr Mater* 2020;183:111-6.  DOI

13.  Mukhopadhyay S, Pandey P, Baler N, Biswas K, Makineni SK, Chattopadhyay K. The role of Ti addition on the evolution and stability of γ/γ' microstructure in a Co-30Ni-10Al-5Mo-2Ta alloy. *Acta Mater* 2021;208:116736.  DOI

14.  Liu P, Huang H, Wen C, Lookman T, Su Y. The γ/γ' microstructure in CoNiAlCr-based superalloys using triple-objective optimization. *npj Comput Mater* 2023;9:1090.  DOI

15.  Liu P, Huang H, Jiang X, et al. Evolution analysis of γ' precipitate coarsening in Co-based superalloys using kinetic theory and machine learning. *Acta Mater* 2022;235:118101.  DOI

16.  Zhuang X, Antonov S, Li W, Lu S, Li L, Feng Q. Alloying effects and effective alloy design of high-Cr CoNi-based superalloys via a high-throughput experiments and machine learning framework. *Acta Mater* 2023;243:118525.  DOI

17.  Boddupalli N, Matchen T, Moehlis J. Symbolic regression via neural networks. *Chaos* 2023;33:083150.  DOI  PubMed

18.  Lundberg S, Lee SI. A unified approach to interpreting model predictions. arXiv 2017;arXiv:1705.07874. Available from: https://arxiv.org/abs/1705.07874. [Last accessed on 21 Dec 2024]

19.  Garreau D, Luxburg U. Explaining the explainer: a first theoretical analysis of LIME. arXiv 2020;arXiv: 2001.03447. Available from: https:// arxiv.org/abs/2001.03447. [Last accessed on 21 Dec 2024]

20.  Xiong J, Bai B, Jiang H, Faus-golfe A. Determinants of saturation magnetic flux density in Fe-based metallic glasses: insights from machine-learning models. *Rare Met* 2024;43:5256-67.  DOI

21.  Xiong J, Lei T, Fu D, Wu J, Zhang T. Data driven discovery of an analytic formula for the life prediction of Lithium-ion batteries. *Prog Nat Sci Mater Int* 2022;32:793-9.  DOI

22.  Xiong J, Zhang T, Shi S. Machine learning of mechanical properties of steels. *Sci China Technol Sci* 2020;63:1247-55.  DOI

23.  Xiong J, Shi S, Zhang T. A machine-learning approach to predicting and understanding the properties of amorphous metallic alloys. *Mater Des* 2020;187:108378.  DOI

24.  Meher S, Nag S, Tiley J, Goel A, Banerjee R. Coarsening kinetics of γ' precipitates in cobalt-base alloys. *Acta Mater* 2013;61:4266-76.  DOI

25.  Zhou H, Xue F, Chang H, Feng Q. Effect of Mo on microstructural characteristics and coarsening kinetics of γ' precipitates in Co–Al–W–Ta–Ti alloys. *J Mater Sci Technol* 2018;34:799-805.  DOI

26.  Chen Y, Wang C, Ruan J, et al. Development of low-density γ/γ' Co–Al–Ta-based superalloys with high solvus temperature. *Acta Mater* 2020;188:652-64.  DOI

27.  Chen Y, Wang C, Ruan J, et al. High-strength Co–Al–V-base superalloys strengthened by γ'-Co$_3$(Al,V) with high solvus temperature. *Acta Mater* 2019;170:62-74.  DOI

28.  Vorontsov V, Barnard J, Rahman K, Yan H, Midgley P, Dye D. Coarsening behaviour and interfacial structure of γ' precipitates in Co-Al-W based superalloys. *Acta Mater* 2016;120:14-23.  DOI

29.  Zhuang X, Antonov S, Li L, Feng Q. Effect of alloying elements on the coarsening rate of γ' precipitates in multi-component CoNi-based superalloys with high Cr content. *Scr Mater* 2021;202:114004.  DOI

30.  Lifshitz I, Slyozov V. The kinetics of precipitation from supersaturated solid solutions. *J Phys Chem Solids* 1961;19:35-50.  DOI

31.  Ardell AJ, Ozolins V. Trans-interface diffusion-controlled coarsening. *Nat Mater* 2005;4:309-16.  DOI  PubMed

32.  Zhang J, Liu L, Huang T, et al. Coarsening kinetics of γ' precipitates in a Re-containing Ni-based single crystal superalloy during long-term aging. *J Mater Sci Technol* 2021;62:1-10.  DOI

33.  Gusak A, Lutsenko G, Tu K. Ostwald ripening with non-equilibrium vacancies. *Acta Mater* 2006;54:785-91.  DOI

34.  Sun W. Kinetics for coarsening co-controlled by diffusion and a reversible interface reaction. *Acta Mater* 2007;55:313-20.  DOI

35.  Calderon H, Voorhees P, Murray J, Kostorz G. Ostwald ripening in concentrated alloys. *Acta Metall Mater* 1994;42:991-1000.  DOI

36.  Khatavkar N, Singh AK. Combined approach to capture the evolution of oxidation of Nickel based superalloys using data driven approaches. *Phys Rev Mater* 2024;8:053601.  DOI

37.  Wu J, Li Y, Qiao H, Yang Y, Zhao J, Huang Z. Prediction of mechanical properties and surface roughness of FGH4095 superalloy treated by laser shock peening based on XGBoost. *J Alloys Metall Syst* 2023;1:100001.  DOI

38.  Ma C, Tang Y, Bao G. Machine learning-based prediction and generation model for creep rupture time of Nickel-based alloys. *Comput*

*Mater Sci* 2024;233:112736. DOI

39. Mythreyi OV, Srinivaas MR, Amit Kumar T, Jayaganthan R. Machine-learning-based prediction of corrosion behavior in additively manufactured inconel 718. *Data* 2021;6:80. DOI

40. Chen TQ, Guestrin C. XGBoost: a scalable tree boosting system. arXiv 2016;arXiv:1603.02754. Available from: https:// arxiv.org/abs/1603.02754. [Last accessed on 21 Dec 2024]

41. Belkina AC, Ciccolella CO, Anno R, Halpert R, Spidlen J, Snyder-Cappione JE. Automated optimized parameters for T-distributed stochastic neighbor embedding improve visualization and analysis of large datasets. *Nat Commun* 2019;10:5415. DOI PubMed PMC

42. Gan W, Gao H, Wen Z. Based on damage caused by microstructure evolution during long-term thermal exposure to analyze and predict creep behavior of Ni-based single crystal superalloy. *AIP Advances* 2020;10:085301. DOI

43. Qu S, Li Y, Wang C, et al. Coarsening behavior of γ' precipitates and compression deformation mechanism of a novel Co–V–Ta–Ti superalloy. *Mater Sci Eng A* 2020;787:139455. DOI

44. Reed RC. The superalloys: fundamentals and applications. Available from: https://www.researchgate.net/publication/287242590_The_Superalloys_Fundamentals_and_Applications. [Last accessed on 21 Dec 2024].

45. Zhang X, Shang H, Gao Q, et al. Coarsening evolution of γ' phase and failure mechanism of Co-Ni-Al-Ti-based superalloys during isothermal aging. *Front Mater* 2022;9:863305. DOI

46. Shang H, Ma Q, Gao Q, et al. Yield strength anomaly evaluation of W-free Co-Ni-Al-based superalloys during high temperature tensile tests. *Mater Charact* 2022;192:112242. DOI

47. Gao Q, Shang H, Ma Q, et al. Isothermal oxidation behavior of W-free Co–Ni–Al-based superalloy at high temperature. *Mater Charact* 2022;73:513-25. DOI

48. Gao Q, Jiang Y, Liu Z, et al. Effects of alloying elements on microstructure and mechanical properties of Co–Ni–Al–Ti superalloy. *Mater Sci Eng A* 2020;779:139139. DOI